The magnetic moment operator reproducing these matrix elements in the selected four-dimensional $J = 0, 1$ subspace can be written down in an elegant way

$$\boldsymbol{M} = 2\boldsymbol{S} - \boldsymbol{L}^{\text{eff}} = -\sqrt{6}\, i(s^\dagger \boldsymbol{T} - \boldsymbol{T}^\dagger s) - \tfrac{1}{2}\, i(\boldsymbol{T}^\dagger \times \boldsymbol{T})\,. \tag{2.90}$$

In this form it is clear that the major potential to generate a magnetic moment have the transitions between s and $\boldsymbol{T}$ states, the second part is the already mentioned contribution of the $\boldsymbol{J}$ moment of the triplet that is equivalent to $-i(\boldsymbol{T}^\dagger \times \boldsymbol{T})$ within the $J = 0, 1$ subspace.

2.3 Electronic hopping and tight-binding approximation

So far we have been dealing with the (rather complex) physics of correlated valence shells of the individual ions. In this section we are going to activate connections between the ions in the form of electronic hopping. There will not be any many-body aspects discussed here as our main goal is just to get the matrix elements enabling a single electron to move from site to site – so-called tight-binding parameters entering a single-electron hopping Hamiltonian. As a motivating example we start by considering independent electrons moving in a crystal consisting of identical atoms arranged in a simple lattice. Their wavefunctions obey the Schrödinger equation

$$\left[-\frac{\hbar^2}{2m}\nabla^2 + \sum_{\boldsymbol{R}} V_{\text{at}}(\boldsymbol{r} - \boldsymbol{R})\right] \Psi = E\Psi\,, \tag{2.91}$$

where $V_{\text{at}}(\boldsymbol{r} - \boldsymbol{R})$ is the atomic potential for an atom placed at site $\boldsymbol{R}$. Summed through the lattices sites, the atomic potentials generate a periodic crystal potential. In the tight-binding approximation to the problem (2.91), one assumes that the relevant states are well localized so that the electron wavefunctions can be constructed as linear combinations of atomic orbitals. This concept is illustrated by Fig. 16 where we construct a virtual two-dimensional crystal made out of potential wells of circular symmetry and study the evolution of its energy levels when reducing the lattice spacing, i.e. bringing the initially isolated atoms closer to each other. At very large lattice spacing, the spectrum of energy levels has a discrete structure below the top of the crystal potential, corresponding to the individual bound states of the isolated wells. Above that threshold energy, delocalized states forming a continuum are found. As we bring the "atoms" closer and closer, the localized states start to overlap and their interaction produces energy bands of increasing bandwidth. The higher-energy bound states are forming bands sooner because they have a larger spatial extent and overlap more easily. This is an analogy of the atomic orbitals in a crystal - the valence ones form bands while the deep electron levels retain their atomic character. It is intuitively clear that in the situation with rather well localized states (the electrons are "tightly bound" to their atoms), the appropriate model Hamiltonian should be of the form

$$\mathcal{H}_{\text{TB}} = \sum_{n\boldsymbol{R}} \left[\varepsilon_n\, c^\dagger_{n\boldsymbol{R}} c_{n\boldsymbol{R}} - \sum_{n'\Delta\boldsymbol{R}} t_{nn'}(\Delta\boldsymbol{R})\, c^\dagger_{n',\boldsymbol{R}+\Delta\boldsymbol{R}}\, c_{n\boldsymbol{R}}\right]\,, \tag{2.92}$$

where the operators $c^\dagger_{n\boldsymbol{R}}$ and $c_{n\boldsymbol{R}}$ create/annihilate an electron in the state $|\phi_{n\boldsymbol{R}}\rangle$ corresponding to orbital n at site $\boldsymbol{R}$. The first part of this tight-binding Hamiltonian $\mathcal{H}_{\text{TB}}$ just counts the energies of the occupied orbitals [c.f. the energies ε_α in (2.46)], the second part captures the hopping of electrons between the orbitals located at $\boldsymbol{R}$ and $\boldsymbol{R} + \Delta\boldsymbol{R}$. The amplitudes of the hopping processes are the matrix elements of the original crystal Hamiltonian such as that of Eq. (2.91): $t_{nn'}(\Delta\boldsymbol{R}) = -\langle\phi_{n',\boldsymbol{R}+\Delta\boldsymbol{R}}|\,\mathcal{H}\,|\phi_{n\boldsymbol{R}}\rangle$. The signs are introduced in such a way that the hopping parameters t will be mostly positive. For the sake of brevity, we ignore spin that is

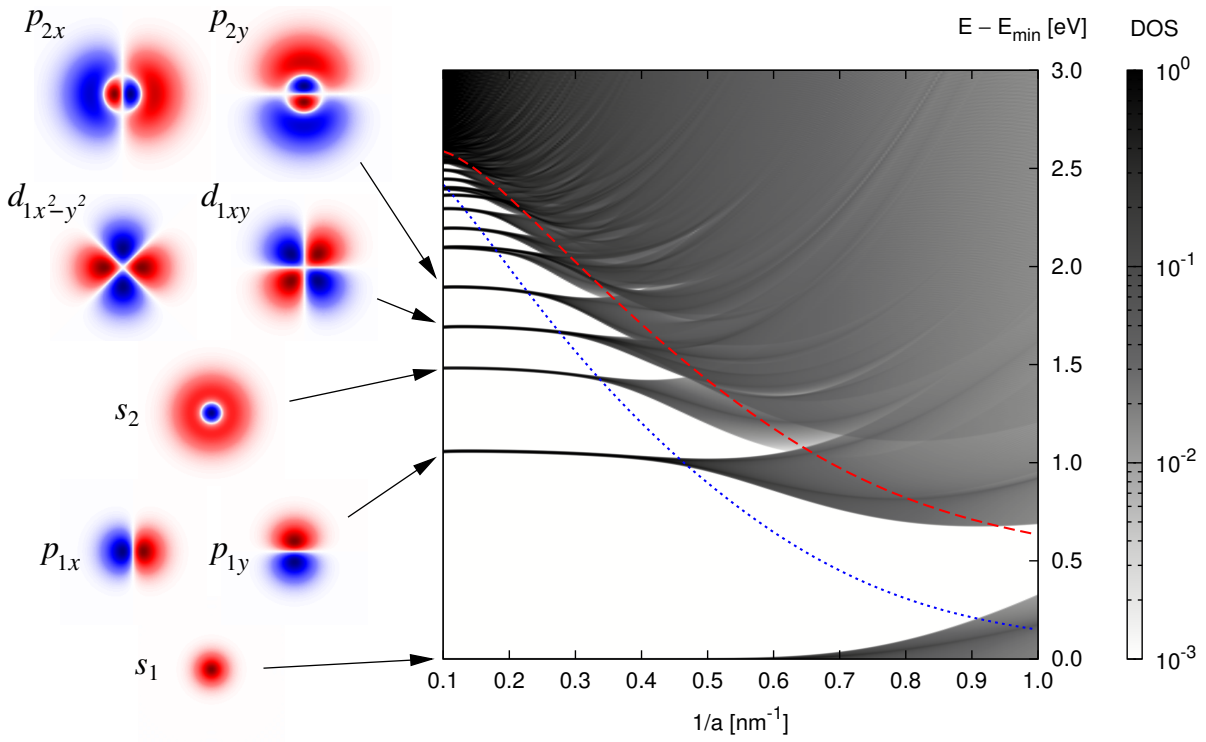

Fig. 16: (left) Wavefunctions of the lowest eigenstates in the potential well described by the 2D potential $V_{\rm at}(r) = V_0 \exp(-\kappa r)\, r_0/(r + r_0)$ with $V_0 = 5\,$eV, $\kappa = 0.5\,$nm^{-1}, $r_0 = 0.5\,$nm. The indicated levels are either non-degenerate or two-fold degenerate and they are labeled in analogy with atomic orbitals. (right) Density of states for a square lattice of the above wells as function of the inverse lattice spacing $1/a$. The energy is measured from the lowest eigenstate. For a large spacing (small $1/a$) the wells are practically isolated and the density of states shows discrete peaks at the energies of bound states. Blue dotted line indicates the average potential level, the red dashed line the top of the potential. The data to construct this figure were obtained by solving Eq. (2.91) by plane-wave expansion method.

conserved during the hopping and would come as an extra index σ together with $\sum_\sigma$. While the values of hopping amplitudes are not known yet, one can expect that the nearest-neighbor and possibly second nearest-neighbor ones will be most important and – in the case of more orbitals involved – also anticipate their symmetry structure [see Fig. 17(a) and (b) for two examples].

Owing to the periodicity of the lattice, the Hamiltonian can be easily diagonalized by employing Bloch waves assembled as linear combinations of the atomic orbitals:

$$|n\boldsymbol{k}\rangle = \frac{1}{\sqrt{N}} \sum_{\boldsymbol{R}} \mathrm{e}^{i\boldsymbol{k}\cdot\boldsymbol{R}}\, |\phi_{n\boldsymbol{R}}\rangle\,. \tag{2.93}$$

Here N denotes the total number of sites in the crystal and normalizes $|n\boldsymbol{k}\rangle$ to unity when the overlaps of orbitals at different sites are negligible. By inserting the consistently transformed electron operators $c_{n\boldsymbol{R}} = N^{-1/2} \sum_{\boldsymbol{k}} \mathrm{e}^{i\boldsymbol{k}\cdot\boldsymbol{R}} c_{n\boldsymbol{k}}$ into $\mathcal{H}_{\rm TB}$, it acquires the form with separated contributions of the individual Bloch vectors $\boldsymbol{k}$

$$\mathcal{H}_{\rm TB} = \sum_{\boldsymbol{k}} \sum_{nn'} \left[\varepsilon_n \delta_{nn'} - \sum_{\Delta\boldsymbol{R}} t_{nn'}(\Delta\boldsymbol{R})\, \mathrm{e}^{-i\boldsymbol{k}\cdot\Delta\boldsymbol{R}} \right] c^\dagger_{n'\boldsymbol{k}} c_{n\boldsymbol{k}}\,. \tag{2.94}$$

For each $\boldsymbol{k}$, it remains to diagonalize a matrix whose dimension is equal to the number of orbitals involved (no diagonalization is thus needed in case of one relevant orbital). For the two examples

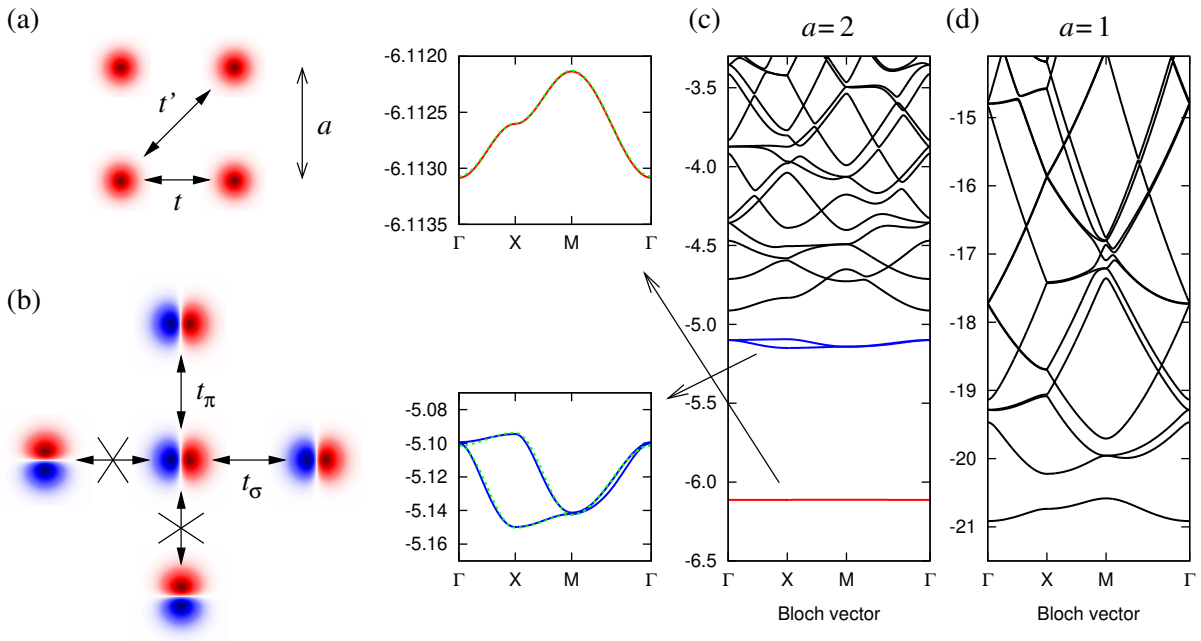

Fig. 17: (a) Hopping processes included in the simplest tight-binding approximation for the bands derived from s "orbitals" of Fig. 16 in a square lattice. Nearest-neighbor and next nearest-neighbor hopping amplitudes t and t' are indicated. (b) Hopping processes involving the p orbitals on a square lattice. The symmetry of these states makes certain hopping amplitudes to vanish, the non-zero ones depend on the relative orientation of the orbitals (t_σ and t_π). (c) Band structure obtained for the setup of Fig. 16 and the value $a = 2\,\mathrm{nm}$ of the lattice parameter. The weakly dispersing bands derived from the s_1 and p_1 levels are shown in detail on the left. The green dashed lines are fits by the corresponding nearest-neighbor tight-binding dispersion relations. The band structure is plotted along the conventional path involving $\Gamma = (0,0)$, $\mathrm{X} = (\pi/a, 0)$ and $\mathrm{M} = (\pi/a, \pi/a)$ points in the Brillouin zone. (d) Band structure for $a = 1\,\mathrm{nm}$ where even the lowest level already shows a significant dispersion. Its profile seems to be just a scaled version of that from panel (c), demonstrating the applicability of the tight-binding scheme.

in Fig. 17(a),(b) we get

$$\mathcal{H}_{\mathrm{TB}} = \sum_{\boldsymbol{k}} \left[\varepsilon_s - 2t(\cos k_x a + \cos k_y a) - 4t' \cos k_x a \cos k_y a\right] c^\dagger_{\boldsymbol{k}} c_{\boldsymbol{k}} \tag{2.95}$$

and

$$\mathcal{H}_{\mathrm{TB}} = \sum_{\boldsymbol{k}} \begin{pmatrix} c^\dagger_{p_x \boldsymbol{k}} & c^\dagger_{p_y \boldsymbol{k}} \end{pmatrix} \begin{pmatrix} \varepsilon_p - 2t_\sigma \cos k_x a - 2t_\pi \cos k_y a & 0 \\ 0 & \varepsilon_p - 2t_\pi \cos k_x a - 2t_\sigma \cos k_y a \end{pmatrix} \begin{pmatrix} c_{p_x \boldsymbol{k}} \\ c_{p_y \boldsymbol{k}} \end{pmatrix} \tag{2.96}$$

giving directly the dispersion relations of electrons. In the latter case, nonzero off-diagonal elements would be generated by next nearest-neighbor hopping, nearest-neighbor pairs of p_x and p_y orbitals are not connected due to symmetry reasons. The band structures obtained numerically by solving the full problem (2.91) are presented in Fig. 17 and contrasted to those resulting in nearest-neighbor tight-binding approximation. A remarkable agreement is obtained when choosing the proper values of the few parameters (ε_s and t or ε_p and t_σ, t_π), in particular for the s band derived from the most localized bound state.

As we have just seen, the tight-binding approximation is a useful tool well capturing the dispersion of the bands derived from localized states. Its success relies on a limited range of

significant overlaps (in the sense of the matrix element of $\mathcal{H}$) of those localized states, reaching only few nearest neighbors. Our motivational example was based on a collection of weakly coupled atoms. However, single-electron problems similar to Eq. (2.91) also arise as auxiliary problems in *ab-initio* calculations within the framework of density functional theory (DFT). There exist sophisticated approaches how to construct the local orbital bases such as maximally localized Wannier orbitals and to extract the values of the corresponding hopping matrix elements making the tight-binding scheme applicable in a broader context. In a way, by considering the limit of weakly coupled atoms, we obtain hints about the symmetry/structure of the corresponding tight-binding model, a realistic DFT calculation then fills in the actual values of the parameters.

After the initial exposition of the tight-binding approach, we will now focus in more detail on the symmetry properties of the tight-binding matrix elements $t_{nn'}(\Delta\boldsymbol{R}) = -\langle\phi_{n',\boldsymbol{R}+\Delta\boldsymbol{R}}|\,\mathcal{H}\,|\phi_{n\boldsymbol{R}}\rangle$. for transition metal compounds. The relevant ones are those connecting an oxygen ion and a transition metal ion (i.e. p and d orbitals), and two transition metal ions (only d orbitals involved). A general approach of their symmetry reduction to as few parameters as possible under the assumption of spherically symmetric atomic wavefunctions[9] was developed by Slater and Koster [33]. Let us write down the matrix element $t_{nn'}(\Delta\boldsymbol{R})$ explicitly

$$t_{nn'}(\Delta\boldsymbol{R}) = -\int \phi^*_{n'}(\boldsymbol{r}-\Delta\boldsymbol{R})\left[-\frac{\hbar^2}{2m}\nabla^2 + \sum_{\boldsymbol{R}'} V_{\mathrm{at}}(\boldsymbol{r}-\boldsymbol{R}')\right]\phi_n(\boldsymbol{r})\,\mathrm{d}^3\boldsymbol{r}\,. \tag{2.97}$$

We can ignore the on-site elements ($\Delta\boldsymbol{R} = \boldsymbol{0}$), these can be incorporated into the local level structure by renormalizing the energies ε_n. The basic trick is to use the fact that $\phi_n(\boldsymbol{r})$ and $\phi^*_{n'}(\boldsymbol{r}-\Delta\boldsymbol{R})$ are eigenstates of the atomic Hamiltonian $-\frac{\hbar^2}{2m}\nabla^2 + V_{\mathrm{at}}(\boldsymbol{r})$ or $-\frac{\hbar^2}{2m}\nabla^2 + V_{\mathrm{at}}(\boldsymbol{r}-\Delta\boldsymbol{R})$, respectively. This enables a decomposition of the integral in (2.97) into three contributions

$$\begin{aligned} t_{nn'}(\Delta\boldsymbol{R}) = &-\int \phi^*_{n'}(\boldsymbol{r}-\Delta\boldsymbol{R})\left[\tfrac{1}{2}V_{\mathrm{at}}(\boldsymbol{r}) + \tfrac{1}{2}V_{\mathrm{at}}(\boldsymbol{r}-\Delta\boldsymbol{R})\right]\phi_n(\boldsymbol{r})\,\mathrm{d}^3\boldsymbol{r} \\ &-\frac{\varepsilon_n+\varepsilon_{n'}}{2}\int \phi^*_{n'}(\boldsymbol{r}-\Delta\boldsymbol{R})\,\phi_n(\boldsymbol{r})\,\mathrm{d}^3\boldsymbol{r} - \int \phi^*_{n'}(\boldsymbol{r}-\Delta\boldsymbol{R})\sum_{\boldsymbol{R}'\neq\boldsymbol{0},\,\Delta\boldsymbol{R}} V_{\mathrm{at}}(\boldsymbol{r}-\boldsymbol{R}')\,\phi_n(\boldsymbol{r})\,\mathrm{d}^3\boldsymbol{r}\,. \end{aligned} \tag{2.98}$$

We will study just the contribution on the first line and analyze its symmetry for p-d and d-d orbital pairs and spherically symmetric V_{at}. The contributions on the second line – orbital overlaps and a sum of so-called three-center integrals – are usually neglected. In principle, they can be assumed to renormalize the tight-binding parameters.

To evaluate the two-center integrals $\frac{1}{2}\int \phi^*_{n'}(\boldsymbol{r}-\Delta\boldsymbol{R})\,[V_{\mathrm{at}}(\boldsymbol{r}) + V_{\mathrm{at}}(\boldsymbol{r}-\Delta\boldsymbol{R})]\,\phi_n(\boldsymbol{r})\,\mathrm{d}^3\boldsymbol{r}$ one observes that the term in the bracket has a rotational symmetry with $\Delta\boldsymbol{R}$ being the rotational axis. It is therefore convenient to take the decomposition of the orbitals into spherical harmonics

$$\phi_n(\boldsymbol{r}) = f(r)\sum_{m=-l}^{+l} c_m Y_{lm}(\vartheta,\varphi) \tag{2.99}$$

and rotate the angular part to the new set of spherical coordinates ϑ_{rot}, φ_{rot}, where the polar angle ϑ_{rot} is measured from $\Delta\boldsymbol{R}$. This operation amounts to a linear transformation of the set of coefficients c_m. After the transformation, the expression for the two-center integrals contains azimuthal integrals of the type $\int Y^*_{l'm'}(\vartheta'_{\mathrm{rot}},\varphi_{\mathrm{rot}})Y_{lm}(\vartheta_{\mathrm{rot}},\varphi_{\mathrm{rot}})\,\mathrm{d}\varphi_{\mathrm{rot}}$ where we have to distinguish the polar angles $\vartheta'_{\mathrm{rot}}$ and ϑ_{rot} since the origin of the spherical coordinate system differs for the

[9] This means wavefunctions of the form (common radial part) × (linear combinations of spherical harmonics) such as the case explored in Sec. 2.1.

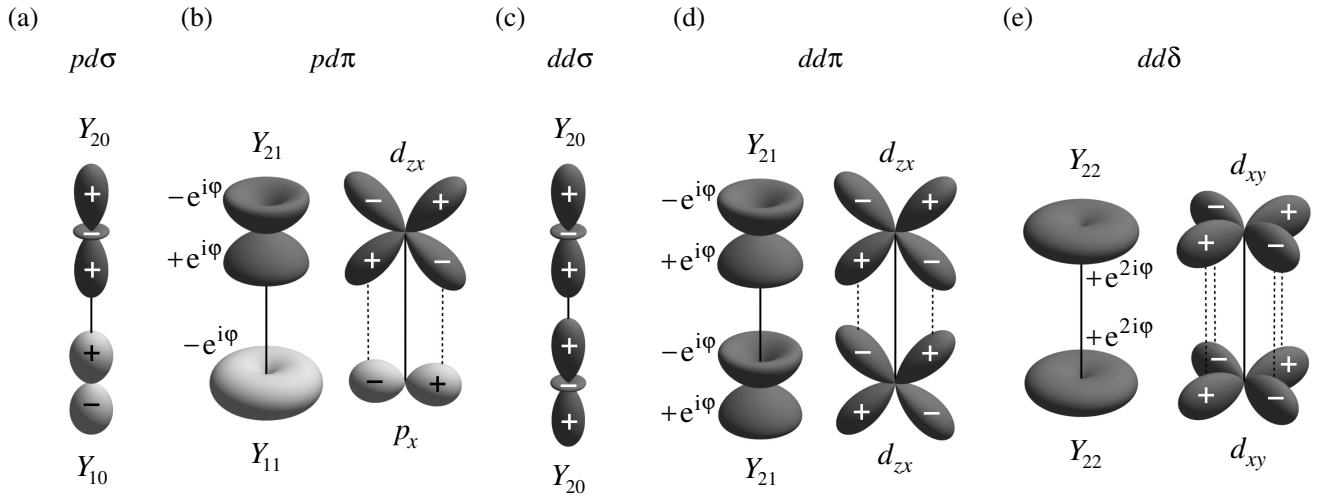

Fig. 18: Illustration of the basic Slater-Koster integrals for p-d and d-d situation. The main rotational axis is z pointing upwards. (a) $(pd\sigma)$ bonding of the in-bond oriented orbitals is the strongest link between p and d orbitals. (b) $(pd\pi)$ bonding is weaker and due to the phases of the spherical harmonics, it comes with an opposite sign to $(pd\sigma)$. A real-orbital example is shown on the right – the integral between p orbital perpendicular to the bond and a matching d orbital is just equal to Slater-Koster $(pd\pi)$, here including the sign. (c) Strongest $(dd\sigma)$ bonding between two d orbitals. (d) Weaker $(dd\pi)$ bonding with the same sign issues as $(pd\pi)$. The integral between the two d_{zx} orbitals shown in the right example is equal to $(dd\pi)$. (e) $(dd\delta)$ bonding and a real-orbital example with the same value of the integral.

two orbitals. The azimuthal angle $\varphi_{\rm rot}$ can be chosen as common. The above integrals vanish for $m' \neq m$ due to the rotational symmetry of the spherical harmonics. The result can thus be expressed as a linear combination of Slater-Koster integrals $(l_1 l_2 m)$ that are defined, following Eq. (2.98), as the two-center integrals $(l_1 l_2 m) = \frac{1}{2}\int \alpha^*(\boldsymbol{r} - \Delta\boldsymbol{R})\,[V_{\rm at}(\boldsymbol{r}) + V_{\rm at}(\boldsymbol{r} - \Delta\boldsymbol{R})]\,\beta(\boldsymbol{r})\,{\rm d}^3\boldsymbol{r}$ with $\beta(\boldsymbol{r}) = f(r)Y_{l_1 m}(\vartheta_{\rm 1rot}, \varphi_{\rm rot})$ and $\alpha(\boldsymbol{r}) = f(r)Y_{l_2 m}(\vartheta_{\rm 2rot}, \varphi_{\rm rot})$. The values of $l_{1,2} = 0, 1, 2, \ldots$ are specified by the conventional letters for atomic orbitals s, p, d, ... and those of $m = 0, 1, 2$ by σ, π, δ, following the chemical bonding nomenclature. Note that the values for $+m$ and $-m$ are identical.

The basic set of Slater-Koster integrals needed for the analysis of hoppings in transition metal oxides is presented in Fig. 18. The main contribution to the Slater-Koster integrals will be presumably collected near the central area of the bond. Taking into consideration the angular distribution of the spherical harmonics, it may be expected that σ bonding is in general stronger than π bonding and that is stronger than δ bonding. One can also anticipate the signs: Since $V_{\rm at}$ is negative, the Slater-Koster integral typically has a negative sign when the closest lobes of the two orbitals have equal signs (or same complex phase). Accordingly, the indicated σ and δ Slater-Koster integrals will be probably negative while the π ones positive. Following our definition, the hopping parameters $t_{nn'}$ will be of opposite signs, for example the hopping t between s orbitals is positive which is indeed observed in Fig. 17. The above "rules of thumb" are useful when inspecting the actual hopping channels between ions as we will do soon. To have a more intuitive notation, we incorporate the anticipated signs into the newly introduced labels for hopping parameters:

$$t_{pd\sigma} = -(pd\sigma)\,, \quad t_{pd\pi} = +(pd\pi)\,, \quad t_{dd\sigma} = -(dd\sigma)\,, \quad t_{dd\pi} = +(dd\pi)\,, \quad t_{dd\delta} = -(dd\delta) \qquad (2.100)$$

that will be used below and that are not always following Eq. (2.98). In this convention the hopping parameter will be taken positively if orbital lobes of the same sign "meet" on the bond.

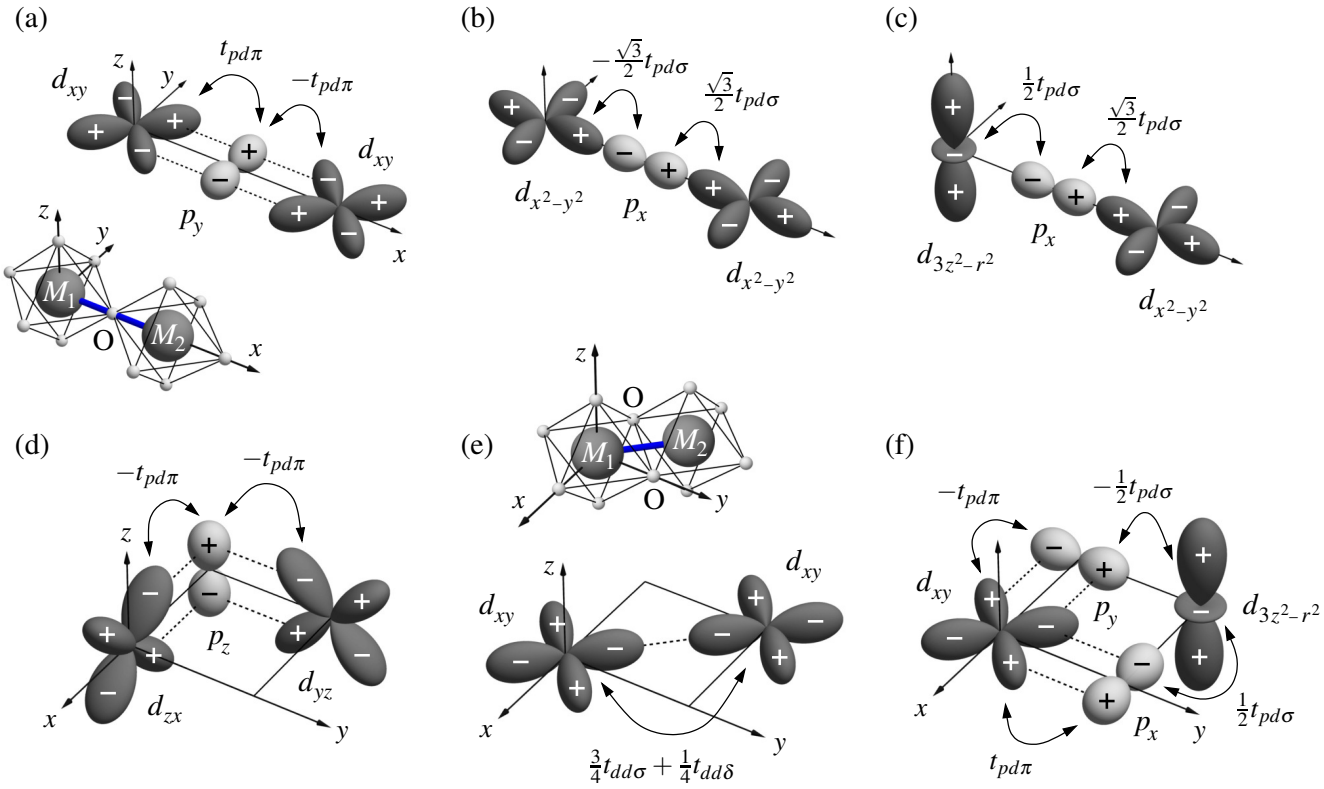

Fig. 19: Examples of hopping channels contributing to nearest-neighbor hopping between two transition metal ions in the case of 180° metal-oxygen-metal bonds (a,b,c) and 90° bonds (d,e,f). The indicated hopping amplitudes use the quantities defined by Eq. (2.100). The insets show the geometry of the connected octahedra and label the transition metal ions by $M_{1,2}$. The setup of the axes for the 90° case is identical to Fig. 7(b),(c) (z-bond). There are a few more contributing options that were not shown: (a) Connection of two d_{zx} orbitals via p_z, (b) connection of two $d_{3z^2-r^2}$ orbitals via p_x, (c) situation with interchanged d orbitals, (d) hopping between d_{zx} and d_{yz} mediated by p_z of the front oxygen of the metal$_2$-oxygen$_2$ plaquette.

When dealing with hoppings in transition metal compounds, we most frequently encounter either 180° metal-oxygen-metal bonds or 90° ones (see e.g. Fig. 1). The various options that we need to consider when connecting two transition metal ions are summarized in Fig. 19. A crucial observation is that e_g orbitals are even when mirrored by any plane containing the bond so that they can only couple to oxygen p orbitals via σ-bonding, while t_{2g} orbitals have an odd-parity mirror plane so that only the π-bonding to oxygen orbitals is possible. As a consequence, the 180° bond geometry enables only separate t_{2g}–t_{2g} and e_g–e_g hoppings, t_{2g}–e_g mixing is absent. For the 90° bond geometry, on the other hand, the t_{2g}–e_g mixing channel is the dominant one and e_g–e_g hopping is forbidden by symmetry. Most of the channels depicted in Fig. 19 correspond to second-order processes involving two successive p-d hoppings. We will now go through the individual cases and inspect the resulting d-d hoppings.

We start with the 180° bond and t_{2g} hopping channel. According to Fig. 19(a) showing an x-bond situation, a pair of d_{xy} orbitals becomes connected through the mediating p_y orbital. The same type of connection, now via p_z orbital, can be found for two d_{zx} orbitals. The remaining t_{2g} orbital d_{yz} is inactive on an x-bond. To derive the effective d-d hopping, we consider the M_1–O–M_2 bond in the initial configuration d^m–p^6–d^n corresponding to a completely filled va-

lence shell of O^{2-}. The process of hopping from the transition metal ion M_1 to M_2 needs to start with a p-d hopping from the oxygen to M_2. This creates a virtual configuration d^m–p^5–d^{n+1} with the excitation energy Δ_{pd} (to be discussed in detail later in Sec. 2.4) that can be relaxed when another electron moves from M_1 to the oxygen and fills the hole in p orbitals. The final configuration is d^{m-1}–p^6–d^{n+1} with one electron moved from M_1 to M_2. Thinking within the framework of the second-order perturbation theory, the amplitude of the whole process can be estimated as $-t_{\mathrm{O}\to 2}t_{1\to\mathrm{O}}/\Delta_{pd}$ which incorporates the amplitudes of the two successive hoppings. The corresponding term in the effective d-d hopping Hamiltonian then reads as $(+t_{\mathrm{O}\to 2}t_{1\to\mathrm{O}}/\Delta_{pd})c_2^\dagger c_1$. The extra sign originates in reordering the electron operators that appear in the sequence $(p^\dagger c_1)(c_2^\dagger p)$ when following the partial hoppings in the perturbation term. Here p, $p^\dagger$ are electron operators corresponding to the participating p orbital. A similar process can be constructed when working out the $2\to 1$ direction of the d-d hopping. Taking into account also the opposite signs of the partial hopping amplitudes observed in Fig. 19(a), we get for the t_{2g} hopping Hamiltonian on the x-bond

$$\mathcal{H}_{ij}^{(x)} = -(t_{pd\pi}^2/\Delta_{pd})(d_{xy}^\dagger d_{xy} + d_{zx}^\dagger d_{zx})_{ij} + \mathrm{H.c.} \tag{2.101}$$

Hopping Hamiltonians for the other bond directions can be obtained by cyclic permutation.

The situation is more complex for e_g orbitals on a 180° bond, where all possible combinations of e_g orbitals are connected. Shown in Fig. 19(b), (c) are two options, there is in addition a connection between two $d_{3z^2-r^2}$ orbitals. Evaluating the effective d-d hopping in this case, we arrive at the bond Hamiltonian

$$\mathcal{H}_{ij}^{(x)} = -\frac{t_{pd\sigma}^2}{\Delta_{pd}} \begin{pmatrix} d_{3z^2-r^2}^\dagger & d_{x^2-y^2}^\dagger \end{pmatrix}_i \begin{pmatrix} +\frac{1}{4} & -\frac{\sqrt{3}}{4} \\ -\frac{\sqrt{3}}{4} & +\frac{3}{4} \end{pmatrix} \begin{pmatrix} d_{3z^2-r^2} \\ d_{x^2-y^2} \end{pmatrix}_j + \mathrm{H.c.} \tag{2.102}$$

For a y-bond the hopping matrix is almost the same, the only change is an opposite sign of the off-diagonal elements as a consequence of the opposite signs of the $d_{x^2-y^2}$ orbital lobes pointing in x and y directions. For a z-bond we have essentially the situation from Fig. 18(a) giving $\mathcal{H}_{ij}^{(z)} = -(t_{pd\sigma}^2/\Delta_{pd})\,(d_{3z^2-r^2}^\dagger d_{3z^2-r^2})_{ij} + \mathrm{H.c.}$ The $d_{x^2-y^2}$ orbital is completely disconnected in that case. The partial hopping amplitude $t_{pd\sigma}$ is typically two times stronger than $t_{pd\pi}$ which makes the e_g hopping more powerful. A well known example of this type of hopping is the motion of holes in the CuO_2 planes of high-T_c cuprates. Residing in the planar $d_{x^2-y^2}$ orbital, they can fully utilize the geometry of the square lattice with Cu–O–Cu bonds.

Moving on to the 90° bond geometry and t_{2g} orbitals, we find that the hopping channel via oxygen is quite similar to the 180° case, with two orbitals out of three being active. However, the path is bent now which results in an *interchange* of t_{2g} orbitals. Specifically, for the bond along $\frac{1}{\sqrt{2}}(y-x)$ direction presented in Fig. 19(d) [the geometry coincides with the z-bonds of Fig. 7(b),(c)], we get

$$\mathcal{H}_{ij} = +(t_{pd\pi}^2/\Delta_{pd})(d_{zx}^\dagger d_{yz} + d_{yz}^\dagger d_{zx})_{ij} + \mathrm{H.c.} \tag{2.103}$$

with the two contributions being mediated separately by the two oxygen ions in the M_2O_2 plaquette. In this geometry there might also be a significant direct overlap of d_{xy} orbitals as shown in Fig. 19(e). For the other two t_{2g} orbitals, a direct hopping is also possible but weak because its matrix element contains $\frac{1}{2}(dd\pi)$ while the d_{xy} orbital uses stronger $\frac{3}{4}(dd\sigma)$. The orbitals active in oxygen-mediated hopping and direct hopping are thus basically complementary. As before, we can get the t_{2g} hoppings for the other bond directions by cyclic permutation.

Finally, let us consider the t_{2g}–e_g hopping on a 90° bond. As demonstrated in Fig. 19(f), the necessary orientation of the p orbitals is only compatible with the d_{xy} orbital. When connecting it to the e_g orbital, an interesting quantum interference effect occurs. For the $d_{3z^2-r^2}$ orbital the two

hopping channels via front and rear oxygen ions come with the same total phases accumulated from the partial p-d hoppings so that they add up to

$$\mathcal{H}_{ij} = +(t_{pd\sigma}t_{pd\pi}/\Delta_{pd})(d^\dagger_{3z^2-r^2}d_{xy} + d^\dagger_{xy}d_{3z^2-r^2})_{ij} + \text{H.c.} \tag{2.104}$$

However, for the $d_{x^2-y^2}$ orbital with alternating signs of its lobes, the amplitudes of the two channels add to zero and $d_{x^2-y^2}$ is thus disconnected. The Hamiltonians for the other bond directions may be obtained by cyclic permutation but in this case a subsequent decomposition of the resulting $d_{3x^2-r^2}$ and $d_{3y^2-r^2}$ e_g orbitals into the conventional $d_{x^2-y^2}$ and $d_{3z^2-r^2}$ pair is needed.

2.4 Mott limit and interactions emerging from residual hopping

Having explored both the physics of the individual ions as well as the way how to connect them via electronic hopping, we are now in position to assemble all together in a form of so-called multiorbital Hubbard model

$$\mathcal{H} = \sum_i \mathcal{H}_{\text{ion}}(i) + \sum_{\langle ij\rangle} \mathcal{H}_{\text{hopping}}(ij)\,. \tag{2.105}$$

The first sum goes through the lattice sites and collects the intra-ionic contributions $\mathcal{H}_{\text{ion}} = \sum_{\alpha\sigma}\varepsilon_\alpha n_{\alpha\sigma} + \mathcal{H}_{\text{Coul}} + \mathcal{H}_{\text{SOC}}$ that we have thoroughly analyzed in Secs. 2.1 and 2.2. The second sum runs through the bonds (quite often nearest-neighbor ones but further neighbors can be included if needed) and activates the various hopping channels as introduced in Sec. 2.3.

At a closer inspection the problem defined by Eq. (2.105) looks intricate and it indeed is. Without $\mathcal{H}_{\text{Coul}}$ we would be just facing a band-structure calculation on a single-electron level, readily performed by an application of the Bloch theorem. However, electron correlations due to two-body interactions contained in $\mathcal{H}_{\text{Coul}}$, that we assume to be strong, make it a genuine many-body problem.[10] We have already successfully handled the electron correlations when diagonalizing the individual $\mathcal{H}_{\text{ion}}$ which was a relatively simple task due to a limited Hilbert space of an individual ion with given number of electrons. This is no more true for a lattice of connected ions since the Hilbert space dimension grows in a terrifying way – essentially exponentially with the number of lattice sites. Moreover, the base for this exponential is not small due to several orbitals involved and combined with spin-$\frac{1}{2}$. When resorting to a fully numerical diagonalization, even the huge computational power easily accessible nowadays enables to exactly treat clusters with a few transition metal ions only.

One way out is to simplify the model by identifying the relevant ionic states – typically the low-energy multiplet states – and formulate an effective model in terms of those. The actual model may be obtained, for example, by getting rid of the high-energy states in a perturbative manner. A proper choice of the elementary objects for the model and processes to be included can make the physics behind the particular material more transparent and guide further approximations. Even though the results may be qualitative only, the insights gained are sometimes more valuable than a quantitative treatment of the original Hubbard model by some complex numerical method.

Our focus is on models with localized degrees of freedom appearing as effective models for undoped Mott insulators, the canonical example being a spin model. In the introductory section 1.2 we took a very simplistic approach to the problem of its emergence. The aim of the present section is to put it on a bit more solid ground to get ready for a derivation of "realistic" models in Secs. 3 and 4.

[10] In principle, there are also inter-ionic interactions of two-body character that could be included in the model, such as Hubbard repulsion of the electrons residing at neighboring ions, but these are only needed in special situations and we do not need to address them in our cases of interest. Consequently, the only source of correlated behavior of electrons in our models will be the intra-ionic electron-electron interactions in $\mathcal{H}_{\text{Coul}}$.